

Probing charge density in materials with atomic resolution in real space

Christopher Addiego¹, Wenpei Gao **©**² ⋈, Huaixun Huyan³ & Xiaoqing Pan **©**^{1,3,4,5} ⋈

Abstract

The charge distribution in materials at the nanoscale can often explain the origin of macroscopic properties such as localized conductivity or the plasmonic response and illuminate more fundamental changes in the microscopic structure such as changes in chemical bonding characteristics. Previously, direct visualization of the charge density with high spatial resolution was often a missing link in the formation of structure–property relationships, especially in heterogeneous materials systems. However, recent advancements in microscopy technology have enabled researchers to visualize the charge distribution in materials down to subatomic length scales. In this Technical Review, we discuss the developments in high-resolution real-space charge distribution imaging using diffraction techniques and electron microscopy, with a focus on the recent advancement of four-dimensional scanning transmission electron microscopy, electron holography, and applications to materials interfaces.

Sections

Introduction

Quantitative convergent beam electron diffraction

Charge density imaging by electron wave phase retrieval

Visualization of charge in materials

Outlook

¹Department of Physics and Astronomy, University of California, Irvine, CA, USA. ²Department of Materials Science and Engineering, North Carolina State University, Raleigh, NC, USA. ³Department of Materials Science and Engineering, University of California, Irvine, CA, USA. ⁴Irvine Materials Research Institute, University of California, Irvine, CA, USA. ⁵Center for Complex and Active Materials, University of California, Irvine, CA, USA. ⊠e-mail: wgao9@ncsu.edu; xiaoqing.pan@uci.edu

Key points

- Real-space charge density imaging can provide key insights into the electronic properties of a material that are unavailable with other methods.
- Transmission electron microscopy can provide high spatial resolution charge images through various methods.
- Quantum crystallography and quantitative convergent beam electron diffraction can reveal the charge distribution in uniform structures with unparalleled accuracy and spatial resolution.
- Phase-retrieval methods provide more direct ways to reveal the charge distribution in heterogeneous materials at atomic resolution in real space.
- Continued development of both microscopy hardware and data analysis techniques will further enhance charge density imaging methods and expand our understanding of materials.

Introduction

Although materials are defined by the atomic species and how they are arranged into crystalline or non-crystalline structures, it is the states and distribution of electrons, especially those in outer orbitals and those forming bonds in between atoms, that determine their properties in chemistry, biology and solid-state physics. The interactions among atoms and the important properties of materials such as localized functionalities in electronic devices, photovoltaic activity in solar cells and catalytic reactions are all mediated by electrons. Thus, visualizing the real-space electronic charge distribution in materials is of critical importance for understanding the properties of materials and devices, especially those phenomena emergent from the interfaces and quantumengineered device structures. However, unlike conventional structural and chemical characterization, measurement of charge at individual defects and interfaces remains a great challenge. In fact, the most common structural characterization techniques in X-ray, neutron scattering and electron microscopy analyse the nanoscale structure by profiling the electromagnetic interactions mostly from the inner shell (core) electrons and the nucleus itself, not the valence electrons that participate in bonding or form the basis for macroscopic properties.

In the past decade, several techniques have seen substantial advancement toward imaging the nanoscale electronic charge distribution in materials, including the contribution of valence electrons. There are two classes of high spatial resolution techniques: quantum crystallography (which not only has its origin in X-ray diffraction but also includes quantitative convergent beam electron diffraction (QCBED))¹⁻³ and then phase-retrieval methods in transmission electron microscopy (TEM)⁴⁻¹². Quantum crystallography is optimized for measuring the valence electron density with high accuracy in homogeneous materials through careful analysis of diffraction data and has advanced quickly with modern computational resources. Phase-retrieval methods, such as electron holography and four-dimensional scanning transmission electron microscopy (4D-STEM), measure the local electric potential and profile the charge distribution in various heterogeneous materials systems with high spatial resolution by calculating the phase (or gradient of the phase) in a scattered electron wave.

Every step of advancement in precision and spatial resolution has led to a leap in studies of materials physics. In this Technical Review, we study the methods and milestones in the development of experimental measurement on charge density, with a focus on recent advances in 4D-STEM and electron holography methods, followed by a discussion of their similarities, unique advantages and new development in future studies. In addition, other techniques, including electron energy loss spectroscopy in TEM, which probes electronic structure, and scanning probe methods, which can map charge on materials surfaces, are highlighted in Boxes 1 and 2.

Quantitative convergent beam electron diffraction X-ray and electron diffraction

Diffraction techniques, including X-ray, neutron and electron diffraction, are some of the most important tools in modern physics, chemistry and materials science. Most experimental setups in diffraction methods follow a similar design (Fig. 1). With an incident beam illuminating the sample, both diffraction originating from the elastic scattering and signals from the inelastic scattering of X-rays by the sample can be recorded. The scattering pattern can be magnified by simply increasing the virtual length between the scattering event and the recording device. According to Bragg's law, $n\lambda = 2d\sin(\theta)$, structure information confined within the spacing, d, between atomic planes in real space can thus be revealed by analysing the intensities distribution over $\sin \theta/\lambda$ in the scattering pattern in reciprocal space. Although diffraction physics and crystallography are not the focus here, they form the basis of techniques in this Technical Review.

Quantum crystallography and QCBED

To extract the electron distribution around atoms and to reveal the bonding characteristics, quantum crystallography was originally developed with the advancement of both theoretical computation and X-ray diffraction analysis 13 . Owing to the nature of the close correlation between chemical bond and bond charges, the theoretical calculations in quantum crystallography and quantum chemistry are mostly the same 14 , and reviews of quantum chemistry are available in refs. 15,16 . In these calculations, the results from scattering experiments provide not only the validation but also refinement to the results from theory. X-ray diffraction can be applied to probe the charge density around atoms by analysing the changes of the wavefunction caused by the local charge in a crystal. The electromagnetic wave interacts with the electrons more than with the nucleus because electrons are much lighter. The X-ray diffraction pattern is then the sum of the individual wavefunctions Ψ_i of the scattered X-ray from each electron.

Consider the integral form of the wavefunction, $\Psi_{\text{total}} = \int \rho(r) e^{-2\pi i \Delta \mathbf{k} \cdot r} dr$, where $\rho(r)$ is the electron probability density at the location r, \mathbf{k} is the wave vector and $\Delta \mathbf{k}$ is the change in wave vector of the scattered X-ray from the incident one. In this form, the wavefunction is in the format of a Fourier transform of the charge density, $\rho(r)$. In a perfect crystal, the structure factor $F(\Delta \mathbf{k}) = \int_{1}^{N} \rho(r) e^{-2\pi i \Delta \mathbf{k} \cdot r} dr$, with the integration taken over the unit cell, is therefore the Fourier transform of the electron charge density in a unit cell. In experimental diffraction patterns, the intensity for a wave vector $\Delta \mathbf{k} = (h, k, l)$ can be written as $I(\Delta \mathbf{k}) = F(\Delta \mathbf{k}) \cdot F(\Delta \mathbf{k})^*$. For most structural analysis purposes, structure factors can be calculated assuming an independent atom model (IAM), in which the bonding and local chemical environment of each atom are not considered. However, the experimental diffraction patterns do include information regarding these factors; therefore, the difference between the structure factors measured in experiment,

Box 1

Electron energy loss spectroscopy

Electron energy loss spectroscopy (EELS) is another scanning transmission electron microscopy-based technique that is often used for studying the charge distribution in materials. In scanning transmission electron microscopy, EELS is performed by collecting the transmitted electrons that have interacted with the sample and then passing them through a magnetic prism, which spreads the electrons into a spectrum based on their difference in energy from the original high-voltage acceleration set at the source. A set of magnetic lenses is then used to focus this spectrum onto a detector, often a direct electron detector. The change in energy of each electron corresponds to an excitation that has been generated in the sample. Thus it is possible to study a wide variety of material properties in EELS simply by focusing on different energy ranges, including lattice vibrations, plasmonic response, local band-gap measurements and X-ray emissions. Core-loss X-ray excitations are the most important for studying the charge distribution in materials because the energy loss near edge structure of specific X-ray excitations can be correlated with the valence state of specific elements 153 . For example, the titanium $L_{2,3}$ edge has a distinctive structure if Ti has a 2+, 3+ or 4+ valence state 154. The processes that

lead to these changes in spectral features are shared with X-ray absorption spectroscopy, so that the theoretical underpinnings of these interactions are well understood 155-157, but EELS can provide much higher spatial resolution than X-ray absorption spectroscopy because it uses a focused electron probe 158,159. The spatial distribution of different valence states is often mapped with nanoscale spatial resolution by collecting spectrum images, in which an EELS spectrum is collected for every probe position in a raster scan. EELS is not a direct measure of the local charge distribution, like phase-retrieval methods or quantitative convergent beam electron diffraction, so there are some disadvantages associated with it. For example, EELS can only be applied if there is a known correlation between some spectral feature and the valence state for an element in the material. In addition, these correlations can be difficult to establish or quantify as they often change from one element to the other and there are many spectral features with which to draw from 153. However, unlike phase-retrieval methods and quantitative convergent beam electron diffraction, EELS valence mapping has very few requirements for sample geometry, so it can be applied to a greater variety of samples and has therefore seen wide adoption in the study of localized electronic properties 160-169.

 $F(\Delta \mathbf{k})^{\mathrm{EXP}}$, and the structure factors calculated with IAM, $F(\Delta \mathbf{k})^{\mathrm{IAM}}$, can be attributed to the bonding characteristics of the material. Determining $F(\Delta \mathbf{k})^{\mathrm{EXP}}$ from experimental data can be challenging as the complex phase is lost when the intensity is recorded on a camera. In quantum crystallography, the way to overcome this problem, and therefore to derive the charge density, $\rho(r)$, is by fitting the experimental intensity with simulated structure factors from which the charge density can be easily calculated. Besides the IAM, in which the electron density is distributed spherically, multipole models ^{17–19} that consider the influence of surrounding atoms in a crystal are also often utilized as the starting point in the fitting. With the data from X-ray diffraction, the charge densities of transition metals ²⁰, carbon ¹⁹ and molecules ²¹ have been studied, revealing the chemical bonds, electron density polarization and effects of crystal fields on the electron charges in these materials.

In TEM, the electron beam also interacts strongly with nuclear charges because they are charged particles; therefore, the structure factor in electron diffraction includes atomic scattering factors that have contributions from the Coulomb interaction with both the surrounding electron density and the positive nuclear charges. When the electron diffraction patterns are collected using a convergent electron beam, the diffraction spots spread into discs and a convergent beam electron diffraction (CBED) pattern is formed. Compared with X-ray scattering or spot diffraction patterns taken using a parallel electron beam, the intensity within diffraction discs in CBED results from electrons with a range of incident angles, containing much more information of the electron–sample interaction (Fig. 2). The wavefunction of the electrons spans over a range of k_i (incident beam direction) and can be precisely calculated by solving the Schrödinger equation using the Bloch wave method in each diffraction disc. For an electron travelling

in the periodic potential field inside the crystal, the time-independent Schrödinger equation can be written as:

$$(K^2 - (k+g)^2)C_g + \sum_h U_{g-h}C_g = 0,$$

$$\Psi_g(x,y) = \sum_h c_i(x,y)C_g^i(x,y)e^{2\pi i(k^j+g)\cdot r},$$

where C_g is the proportion of the gth Bloch wave, both K and U_{g-n} contain information of the potential field and i corresponds to the direction of the wave vector that contributes to the intensity at position (x,y) in the disc; for details see ref. ²². Because the potential field originates from the charge distribution, solving the equation based on the potential field in the IAM gives the calculated CBED pattern. Fitting the potential (calculated CBED patterns) with experimental CBED patterns offers quantitative and accurate measurement of the structure factor and charge density. In this QCBED technique, multiple iterative fitting methods have been developed and applied to the study of charge density as well as crystal structure and Debye–Waller factors of oxides, metals and semiconductors ^{2,23–29} (Fig. 2b–d).

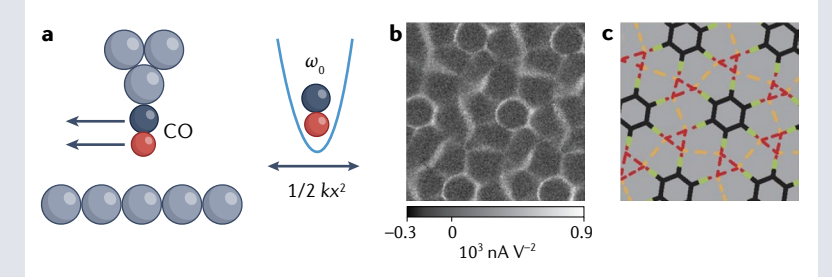
Compared with the structure factor measurement using X-ray diffraction, QCBED considers the dynamic scattering process that allows multiple scattering in a thick crystal sample and does not suffer the same extinction effects of X-ray diffraction, which can reduce the structure factors calculated from low-order diffraction spots. Because CBED is usually taken with a large convergence angle, the electron beam size can be as small as the size of several unit cells, which is smaller than a few nanometres, making it possible to avoid defects and use a small volume of the crystal with uniform bulk structure. The diffraction intensity

Box 2

Scanning probe methods

Although transmission electron microscopy can feasibly characterize the defects, interfaces and other buried heterostructures at atomic resolution in crystalline materials, it is difficult to use when studying surfaces or organic molecules. As transmission electron microscopic images are projections through the entire sample, surface structures can be difficult to resolve. In addition, the beam of high-energy electrons may quickly damage most organic molecules. In comparison, scanning probe microscopy techniques are well suited for studying the electrical properties of surfaces and molecules absorbed onto surfaces^{170,171}. The recent innova usage of functionalized tips in atomic force microscopy. K

molecules absorbed onto surfaces 170,171 . The recent innovation in the usage of functionalized tips in atomic force microscopy, Kelvin probe force microscopy and scanning tunnelling microscopy has enabled the direct imaging of the bonding structure in organic molecules absorbed on surfaces. In these techniques, a small molecule, typically CO, can be absorbed onto the apex of the scanning probe, which greatly enhances the resolution. As the probe scans, changes in the surface potential modify the vibrational mode of the CO molecule (see the figure, part **a**, in which *k* is the local curvature of the vibrational well and ω is the frequency). An image is generated by mapping how various properties of the tip–sample interaction change as the



tip is scanned across the surface. The specific property depends on the exact microscopy technique. In one example using scanning tunnelling microscopy, high-resolution images of the halogen bonds self-assembled halogen-benzene rings were captured by mapping changes in the lateral vibration mode of absorbed CO molecule as the probe was scanned across the sample 172 ; constant current imaging of a self-assembled C_6F_6 island on an Ag (110) surface is shown in the figure (part ${\bf b}$). A schematic diagram with the intermolecular-bonding network highlighted by red and orange dashed lines, indicating the F-3 synthon and trans-type I F···F interaction, is shown in part ${\bf c}$. Figure adapted with permission from ref. 172 , AAAS.

within the CBED discs is the result of electron-sample interaction from a range of incident beam directions, which can be accurately fitted with simulation results using Bloch wave methods, stacked Bloch wave simulations³⁰ and multislice methods³¹. The fitting can be performed using either a strong two-beam condition or the zone axis pattern. In the two-beam condition, the sample and beam are tilted, so that only the transmitted beam and the diffracted beam are excited. The row of diffraction discs appearing in the pattern is called a systematic row. The one-dimensional line profiles of the intensity across the discs in the systematic row from experiments are compared with the calculated one and used to refine the structure factor ^{26,29}. When using the CBED taken along a zone axis, the comparison and fitting are performed using the two-dimensional intensity map of all discs³²⁻³⁶. Recently, QCBED was also developed using off-axis CBED patterns²⁸. More precise quantification can be achieved when QCBED is combined with structure factor measurements from X-ray diffraction, because the latter provides accurate recording of the weak intensity from high-order reflections, which are often missing or noisy in CBED images. With the much-improved accuracy in crystal structure and charge density determination, QCBED has made important contributions to quantum crystallography. The development of QCBED and its applications have been systematically reviewed in refs. 23,36-38.

It is worth noting that because CBED can be done within a small volume defined by the size of the electron beam, local symmetry, strain and atomic structure can be derived using the high-order Laue zone lines. This means that, in principle, QCBED can correlate the bonding characteristics with local structural environment, thus offering high spatial resolution. However, modelling structural heterogeneity and

the associated huge computational cost are obstacles that prevent this approach from being feasible.

Charge density imaging by electron wave phase retrieval

In comparison with the aforementioned techniques in quantum crystallography, methods that directly probe the local charge and its distribution are advantageous to study heterogeneous structures in materials. Despite sharing the same basis of electron-sample interaction in QCBED, the direct methods of imaging the charge density in materials with TEM do not necessarily rely on fitting with simulated results; instead, they use some form of phase retrieval. Phase retrieval is the process of calculating the change in phase of the electron wavefunction after it has interacted with the sample. This task is more challenging than conventional imaging in TEM because the phase of the electron wave cannot be directly recorded on a detector as only the intensity of the wave is recorded. Therefore, the techniques for phase retrieval generally require dedicated hardware and data analysis methods. However, the electron microscopy instrumentation and data analysis methods necessary for phase retrieval have seen considerable advancements in the recent decades, allowing phase retrieval methods to be applied to more complex systems. In this section, we introduce the basics of phase retrieval and cover recent advances in the two most prominent phase-retrieval methods used for studying electronic properties: 4D-STEM and electron holography.

The basis of all phase-retrieval methods lies in the phase-object approximation, which describes the effect of the electrostatic potential of the sample on the incident electron wave. The phase-object approximation can be derived from the Schrödinger equation for the

interaction of a high-energy electron with some simplifying assumptions about the form of the wavefunction and the thickness of the sample. The wavefunction as a function of position, $\Psi(r)$, is assumed to have the form of a product between a plane wave along the beam direction, $e^{i\mathbf{k}z}$, where \mathbf{k} is the wave vector, and another function that varies slowly along the beam direction, $\psi(r)$, such that the full wavefunction can be written as $\Psi(r) = \psi(r)e^{ikz}$. Using this wavefunction with the Schrödinger equation leads to a differential equation with two terms:

$$\frac{\partial}{\partial z}\psi(r) = \left(\frac{i}{2k}\nabla_{\perp}^{2} + i\sigma V(r)\right)\psi(r)$$

where $\nabla_{\!\perp}$ is the Laplacian acting only perpendicular to the beam direction along (x,y), σ is an interaction constant and V(r) is the electrostatic potential of the sample. In this form, we can see that the evolution of the wavefunction can be separated into two parts. The first term on the right describes the propagation of the electron through free space and the second term describes its interaction with the potential of the sample. For this reason, these two terms are often called the propagation and transmission operators, respectively. To solve the wavefunction completely, the two parts must be solved simultaneously. However, if we assume that the sample is very thin, then the propagation through free space can be neglected and the remaining equation can be easily integrated along z, yielding the result of the phase-object approximation:

$$\psi_{\text{exit}} = \psi_o e^{i\sigma V_{\text{proj}}}$$

where $\psi_{\rm exit}$ is the exit wavefunction, ψ_o is the incident wavefunction and $V_{\rm proj}$ is the projected potential of the sample. Thus, determining the phase of the exit wave will tell us about the electrostatic potential in the sample. The charge density can then be calculated from Poisson's equation. For more detailed derivations and full treatments of the electron wavefunction in an electron microscope, see refs. $^{31,39-42}$. Note that the simple phase shift of the incident wave is an essential assumption in all phase-retrieval algorithms, as more complex modifications to the initial wavefunction are exceedingly difficult to parse from experimental data. Samples must be weakly interacting to satisfy these assumptions; for atomic-resolution imaging, this means the phase-object approximation generally is only quantitatively accurate when a sample is thinner than 5–6 nm (ref. 43). For samples with heavy elements, even results from such thin specimen need to be validated by image simulations. Note that QCBED does not assume the weak

phase-object approximation and provides much high accuracy in determining the charge distribution.

4D-STEM and electron holography

4D-STEM is one of the techniques that provide data needed to retrieve the phase of electron wave that has seen innovation in recent years. In 4D-STEM, a converged electron probe is raster-scanned across the sample and a CBED pattern is recorded at each scanning location (Fig. 3a). The CBED can be recorded on a pixelated detector synchronized with the scanning probe. These detectors have been incorporated into many modern electron microscopes owing to the applicability of 4D-STEM towards studying a wide variety of structural, electronic and magnetic properties. The most basic application of 4D-STEM is virtual imaging, in which specific regions of the diffraction pattern are integrated to create different images that highlight specific features, such as regions with different structures, orientations or compositions $^{44-46}$. Strain can also be analysed from low convergence angle 4D-STEM data by measuring the change in the position of diffraction discs^{47,48}. Similarly, polarization can be determined from the internal intensity in outer diffraction discs^{49–51}. The symmetry of diffraction patterns can also be analysed to determine the orientation of a single phase⁵². The pixelated detectors themselves have also seen significant development in recent years. Initially, fast charge-coupled device cameras were typically used to collect 4D-STEM data, but direct electron detectors are becoming increasingly available and can provide much higher quality data at faster frame rates^{53,54}. The fastest direct detectors can now acquire whole diffraction patterns with frame times comparable to the pixel times of conventional STEM detectors⁵⁵⁻⁵⁸. For complete reviews of 4D-STEM, see refs. 59,60.

As the diffraction pattern is a momentum–space image of the probe after interacting with the sample, the change of momentum in the electrons owing to interaction with the sample is encoded in the diffraction data. With a sample that satisfies the phase-object approximation, the gradient of the phase is proportional to the electric field of the sample and can be determined from 4D-STEM data by calculating the average change in momentum of the probe from each diffraction pattern which can be determined from the intensity-weighed average position of the diffraction pattern, also referred to as the centre of mass (COM)⁶. With a full 2D raster scan, a vector map of the electric field can be constructed and then the charge density can be calculated with Gauss' law. Using this technique, the spatial resolution of the charge density image is limited primarily by the size of the electron probe and the step size of the electron probe. The high spatial resolution and the simple process for deriving the electric field and charge

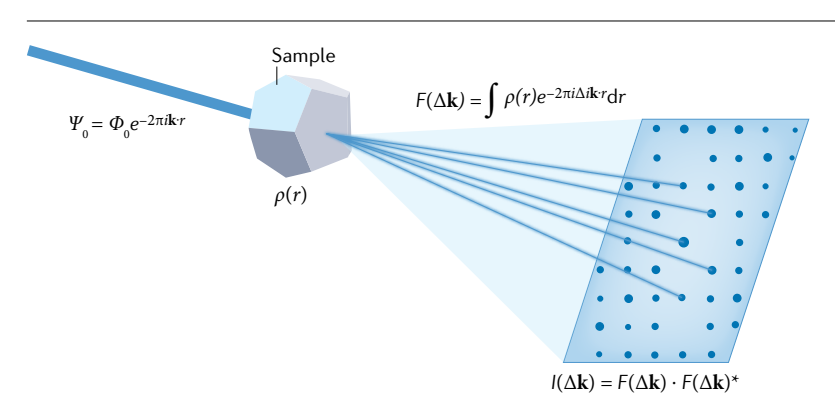


Fig. 1 | **X-ray and electron scattering.** A schematic of the scattering process and the formation of a diffraction pattern applicable to the scattering of both X-rays and electrons. For definitions of variables, please see the main text.

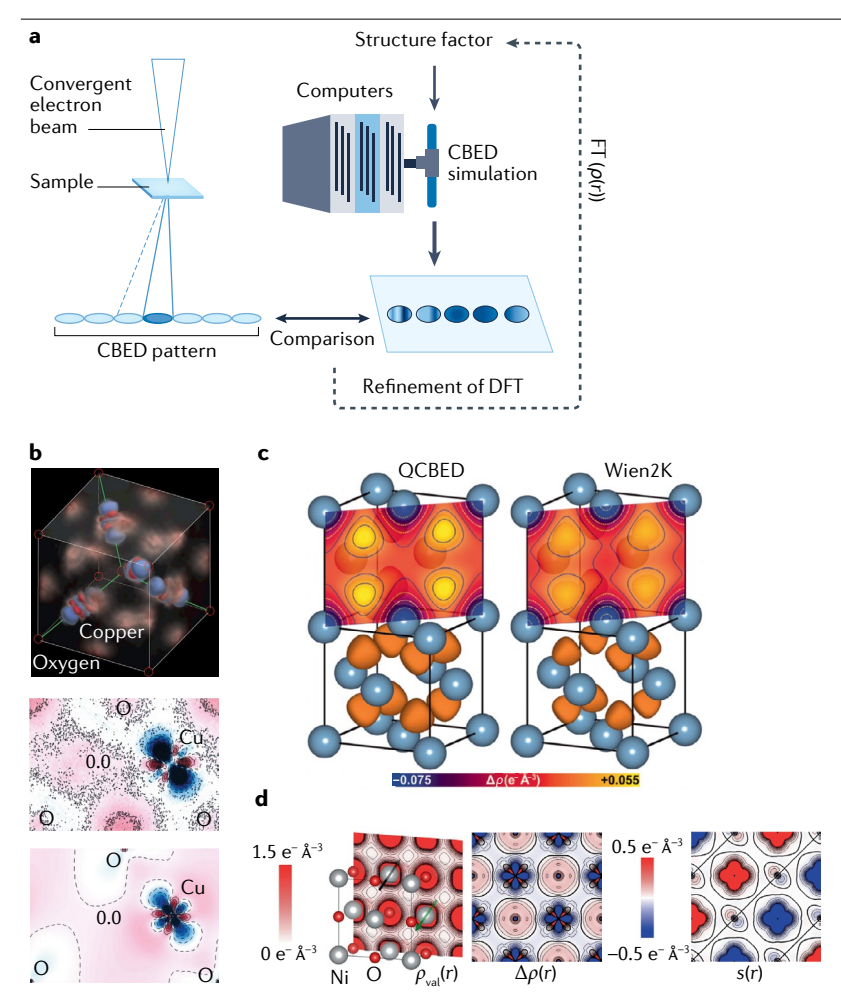


Fig. 2 | **Quantitative convergent beam electron diffraction. a**, A schematic of the workflow for quantitative convergent beam electron diffraction (QCBED). **b**, The direction visualization of *d*-orbital holes and bond charges in Cu₂O using QCBED. **c**, QCBED-derived and density functional theory (DFT) (Wien2K)-derived charge density map of Al. **d**, The determination of the electronic structure of NiO using QCBED-DFT. Panel **b** adapted with permission from ref. ²⁶, Springer Nature Limited. Panel **c** adapted with permission from ref. ², AAAS. Panel **d** adapted with permission from ref. ³ under a Creative Commons licence CC BY 4.0.

density make 4D-STEM ideal for studying heterogeneous structures in materials such as interfaces and defects. An example of the simulated 4D-STEM image of the unit cell of SrTiO₃ and a map of the calculated change in momentum is shown in Fig. 3a. The theory for this technique has been originally conceived 61-63 and developed as differential phase contrast (DPC) imaging, which used segmented conventional detectors instead of pixelated detectors to detect change in probe momentum⁴. The shift of the diffraction pattern can be determined with a segmented detector by examining the difference in the signal collected by opposing detector segments. Theoretical and simulation studies have established that DPC can be used to accurately approximate COM imaging in 4D-STEM⁶⁴⁻⁶⁶. Therefore, even though a segmented detector cannot be used to study the same breadth of material properties as the pixelated detector used in 4D-STEM, for the purposes of charge density/electric field imaging, they are almost equivalent and are often treated as such in experimental studies.

Compared with 4D-STEM, electron holography is a well-established technique for studying electronic properties of materials. Originally proposed in $1948^{67,68}$, holography enables phase reconstruction by modifying the exit wave, so that the wave incident on the detector will carry phase information that is either imaged directly or reconstructed iteratively. This can be done either through interference of the exit wave

with a reference wave of known phase (off-axis holography; Fig. 3b) or by collecting multiple images with a known phase shift between them (in-line holography)⁶⁹. Although the basis for holography has not changed in recent years, atomic-resolution holography has only become routine within the past decade owing to advancements in TEM hardware, including the availability of Cs-correctors, high-brightness sources and direct electron detectors⁷⁰.

Considering the importance of the phase-object approximation for both 4D-STEM/DPC and holography, there are many theoretical and simulation studies exploring its limits and other factors that may affect the final phase (or phase gradient) measurement 43,64-66,71-75. For example, it has been shown in several instances that the probe focal position can have a significant impact on the results in 4D-STEM COM imaging and that focusing the probe below the sample surface can help to mitigate the effects of thicker samples 43,71,74,75. In addition to defocus, other factors in probe formation such as aberrations and convergence angle can also affect the COM image 71,73. Holography is less affected by defocus and other aberrations because they can be corrected after acquisition through forward modelling 12,76. The specific effects of thicker samples such as increased dynamical diffraction and thermal diffuse scattering have also been investigated. It has been found that the effects of dynamical diffraction are more prominent in holography than COM

imaging, whereas the opposite is true for thermal diffuse scattering⁴³. Overall, these theoretical studies have made important contributions to the understanding of how these phase-retrieval techniques can be effectively applied in experiments.

Electron ptychography

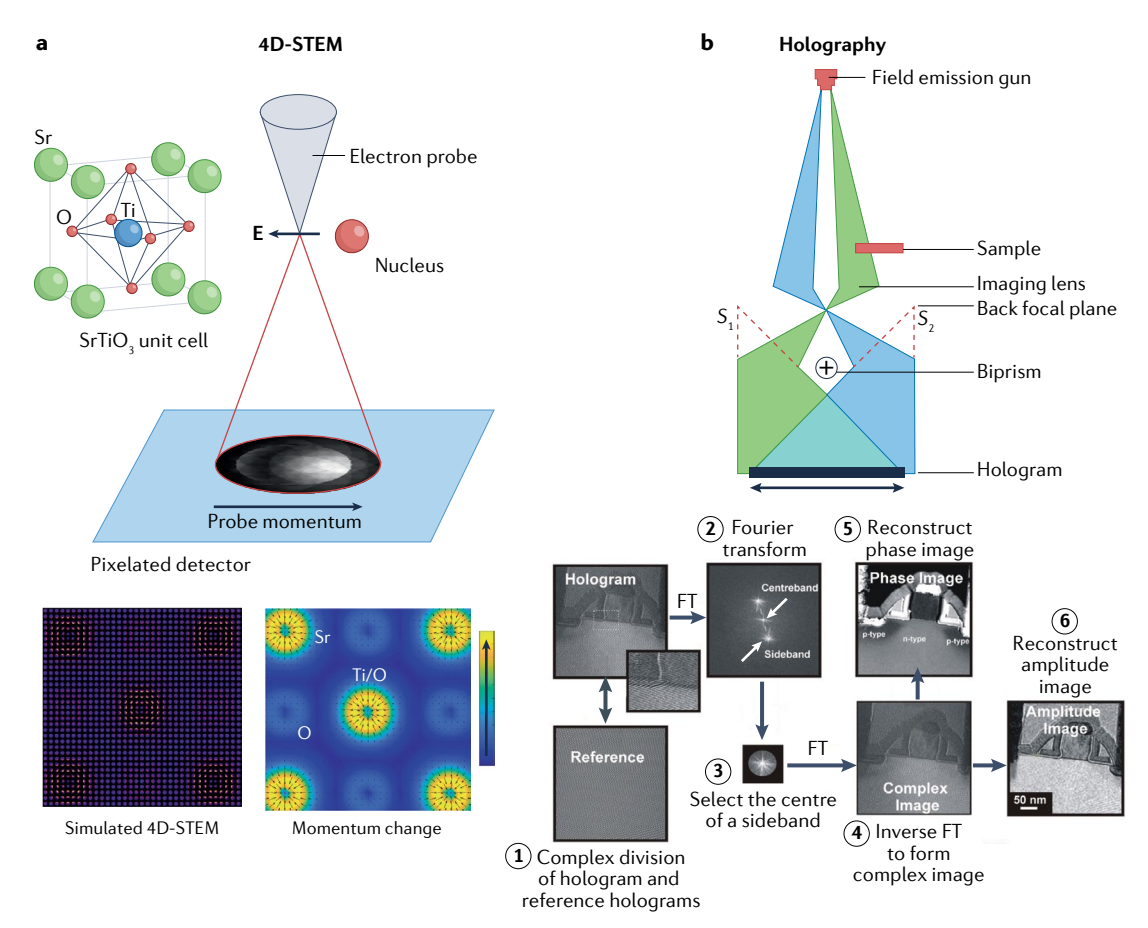
The final prominent phase-retrieval technique in TEM is electron ptychography. Ptychography uses super-sampled 4D-STEM data to perform a full reconstruction of both the probe and the object function⁷⁷, usually through either an iterative algorithm^{78,79} or Wigner distribution deconvolution⁸⁰. Ptvchography has seen wide application as a method for super-resolution, light-element and low-dose imaging⁸¹⁻⁸⁹. Advanced reconstruction algorithms combining multislice forward modelling and ptychographic reconstruction⁸² can even enable 3D imaging of some structures 90. Recently, super-resolution imaging has seen marked advancement, reaching fundamental spatial resolution limits^{91,92}. However, ptychography has not been applied directly to the problem of charge density or electric field imaging, except in a couple of cases^{66,93}, probably owing to its computational complexity. In the cases in which the sample allows for the reconstruction to be completed quickly or already satisfies the phase-object approximation, 4D-STEM/DPC imaging or holography can provide almost the same information with less computational overhead. This faster feedback is especially important in experimental studies of heterostructures as many datasets are often collected during one TEM session. As a result, ptychography is not covered in detail in this Technical Review; for more complete reviews, see refs. 94,95. However, as ptychographic reconstruction algorithms continue to advance and additional computational power becomes available, it is possible that ptychography could be adopted for charge imaging.

Visualization of charge in materials

In this section, we review recent advancements and applications of 4D-STEM and holography in visualizing the charge distribution and other electronic properties in three different types of materials: 2D materials, semiconductors and oxide heterostructures.

2D materials

2D materials often exhibit novel electronic properties because of their unique atomic structure. Although pristine 2D monolayers hold significant promise for applications in electronics ^{96–101}, 2D materials are rarely synthesized without defects ¹⁰². In addition, the defects themselves can often lead to unique properties that are not present in pristine monolayers and thus their own applications. For example, nanopores in graphene may have various applications in chemistry ¹⁰³, and linear defects in transition metal dichalcogenides could provide



 $\label{eq:continuous} \textbf{Fig. 3} \, | \, \textbf{4D} \, \text{scanning transmission electron microscopy and holography.} \\ \textbf{a}, \text{The working principle of the 4D} \, \text{scanning transmission electron microscopy} \\ \text{(STEM) method in mapping the electric field at high spatial resolution.} \, \textbf{E} \, \text{denotes} \\ \\$

the electric field from the nucleus. ${\bf b}$, A diagram of holography in TEM and the workflow for phase retrieval in electron holography. FT, Fourier transform. Panel ${\bf b}$ adapted with permission from ref. 118 , Elsevier.

conductive channels for nanoelectronics 104 . Therefore, it is important to understand the structure and properties of defects, interfaces and other heterostructures in 2D materials. STEM/TEM can provide clear atomic-resolution images of 2D materials 105,106 , which offers structural

information, but electronic properties must be studied with more advanced methods. Owing to the requirement that thin samples be used in phase-reconstruction techniques, 2D materials are a natural fit for 4D-STEM and holography. In addition, conventional spectroscopic

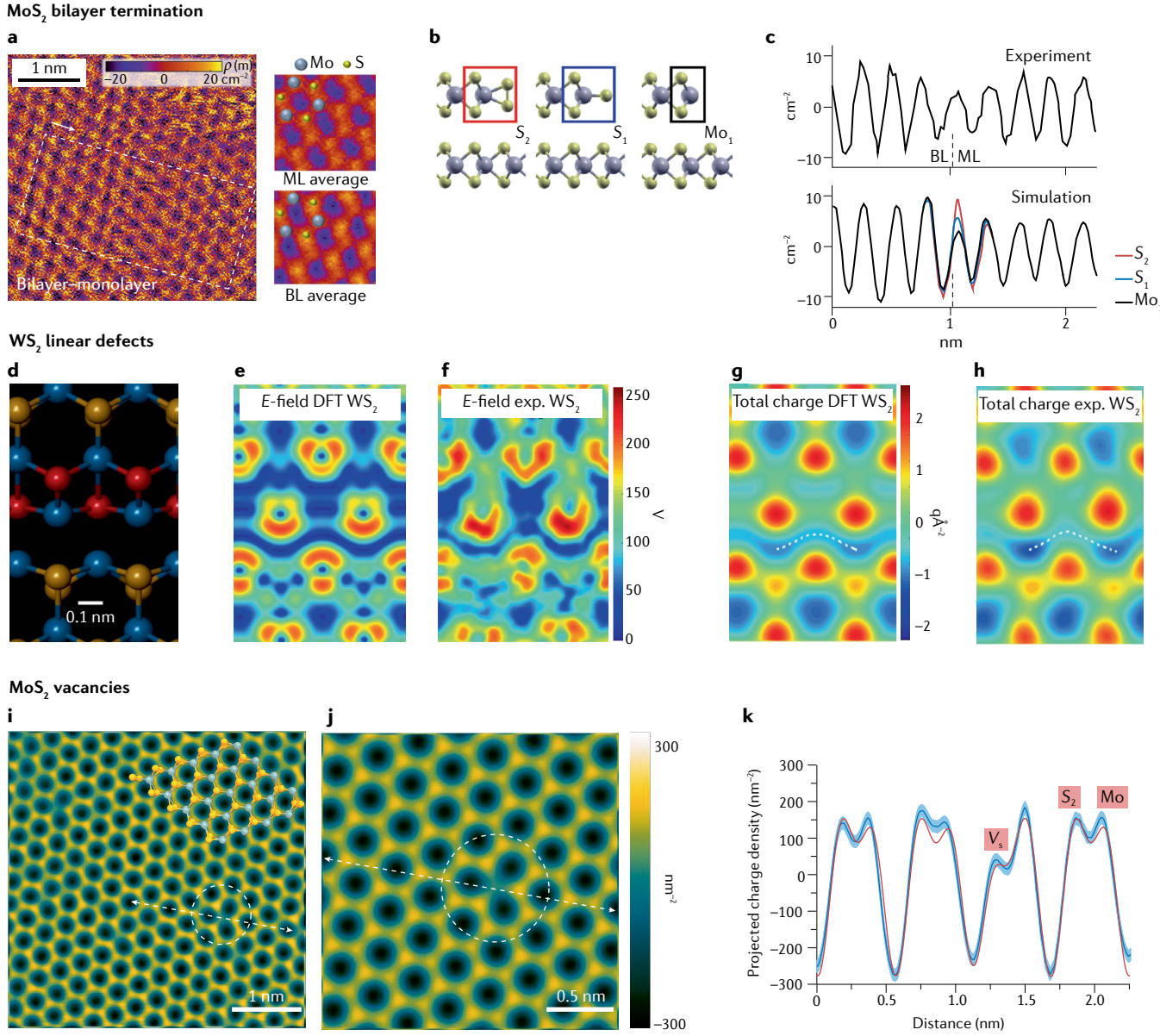


Fig. 4 | **Applications to 2D materials. a**, Charge density image from a monolayer (ML)-bilayer (BL) interface in MoS $_2$ (left) and the average charge density image from ML and BL regions (right). **b**, Strain-minimized atomic models of the termination of the MoS $_2$ ML-BL edge. **c**, Experimental charge density profile taken from the dashed region in part **a** (top) and charge density profiles calculated from multislice image simulations using the structures in part **b** (bottom), indicating that the experimental edge is Mo $_1$ termination. **d**, Atomic model of the W-W bonding region at WS $_2$ line defects. **e**, **f**, Electric field ($|E_L|$) images calculated using DFT (part **e**) and from 4D-STEM experiments (exp.) (part **f**) for WS $_2$. **g**, **h**, The corresponding charge density maps from DFT (part **g**) and the experiment (part **h**). White dashed line indicates the position of a line

profile, see ref. ¹⁰⁴. **i**, Experimental projected charge density of the MoS_2ML calculated from a holography phase image with the structure MoS_2 superimposed, indicating the location of Mo (grey) and S (yellow) atoms. The presence of a V_s defect is indicated. **j**, DFT simulation of the projected charge density of the MoS_2ML with a V_s defect indicated. **k**, Experimental (blue) and simulated (red) profiles of the projected charge density extracted across eight atomic sites including the V_s defect, as indicated by the double arrows in **i**, **j**. Experimental phase error is shown in light blue. Panels **a**-**c** adapted with permission from ref. ¹⁰⁹, APS. Panels **d**-**h** adapted from ref. ¹⁰⁴ under a Creative Commons licence CC BY 4.0. Panels **i**-**k** adapted with permission from ref. ¹¹, ACS.

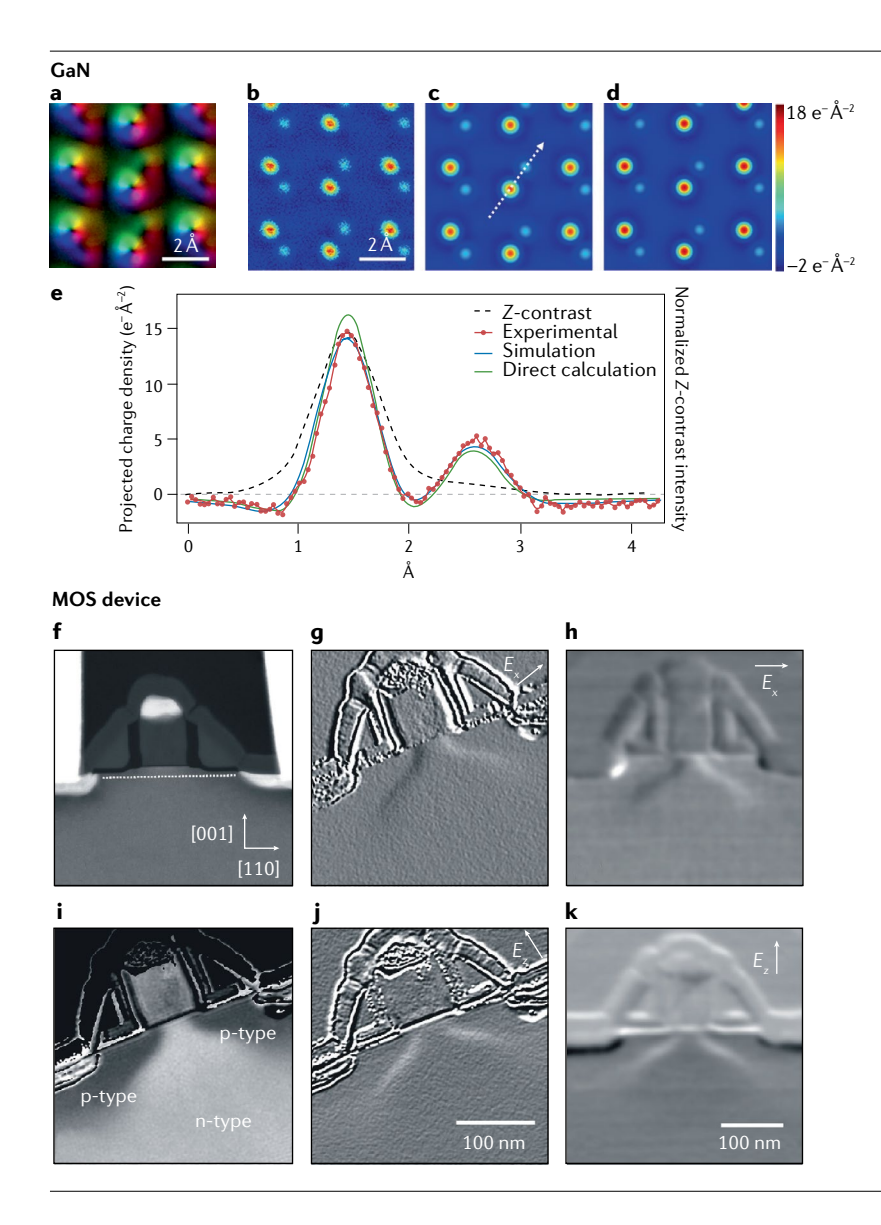


Fig. 5 | Applications to semiconductors. a, Unit-repeatedaveraged image of the projected electric field for GaN down the $[11\overline{2}0]$ direction. The colour and brightness denote the direction and magnitude of the field, respectively. b, Projected charge density map calculated from part a. c.d. Projected charge density image obtained from dynamic electron scattering simulations (part c) and calculated directly from isolated-atom (independent atom model) form factors (part d). The scale bar in panel **b** applies to panels **b**, **c**, and **d**, **e**, Line profiles taken along the white arrow in part c showing the normalized Z-contrast signal profile, experimental, simulated and directly calculated projected total charge density profile. Negative (positive) values represent negative (positive) charge densities. The grey dashed line denotes the zero projected charge. **f**, Scanning transmission electron microscopic image of a silicon p-channel metal-oxide-semiconductor device. g, Potential map acquired from electron holography for the region shown in part **f**. **h**, **i**, Electric field, $E_{\nu}(l)$ and $E_{\nu}(m)$, components calculated from the potential map in \mathbf{g} . \mathbf{j} , \mathbf{k} , Electric field component maps acquired by a low-magnification differential phase contrast imaging. The scale bar in panel j applies to panels g, i and j. The scale bar in panel k applies to panels h and k. Panels a-e adapted with permission from ref.5, ACS. Panels **f-k** adapted with permission from ref. 118, Elsevier.

methods for studying localized electronic properties in TEM, such as electron energy-loss near edge structure, generally require a high beam current and long exposure times to acquire 2D maps because only a small part of the spectrum is used for electron energy loss spectroscopy (EELS) of 2D materials; this often leads to radiation damage in the sample. But such issues can be avoided in 4D-STEM and holography because high-quality data can still be acquired with low beam current and long exposure times when using advanced detectors 107,108.

Initial applications of 4D-STEM electric field and charge density imaging to 2D materials were conducted in 2018, using 4D-STEM to identify the stacking sequence in MoS_2 (ref. 109). Experimental 4D-STEM data are collected from a monolayer–bilayer interface from which the electric field and charge density were calculated (Fig. 4a–c). Several unit cells were averaged together to improve the signal-to-noise ratio in the 2D maps and then compared with the charge density maps and line profiles generated from first principles calculations. The stacking sequence of both pristine bilayer regions and the structure of the

monolayer–bilayer interface were determined with this method. Similar studies of the electric field at the monolayer–bilayer interface of graphene nanopores were also conducted in 2018 110 . These studies demonstrated that electric field and charge density imaging in 4D-STEM is highly sensitive to the atomic structure and specific bonding arrangement of light elements in 2D materials and paved the way for further studies into the electronic structure of 2D materials heterostructures.

In 2019, linear vacancies in MoS_2 and WS_2 were studied using 4D-STEM electric field and charge density imaging ¹⁰⁴. Theoretical studies had predicted that the local band gap in these vacancy channels would decrease to the point where the material becomes metallic and specifically that the metal–metal bond in the vacancies would lead to these channels being electron rich. 4D-STEM results showed that the electron density in these channels matched quantitatively with results from first principles density functional theory (DFT) calculations (Fig. 4d–h). Before the development of 4D-STEM, observing the electron distribution in interatomic regions was not possible in irregular

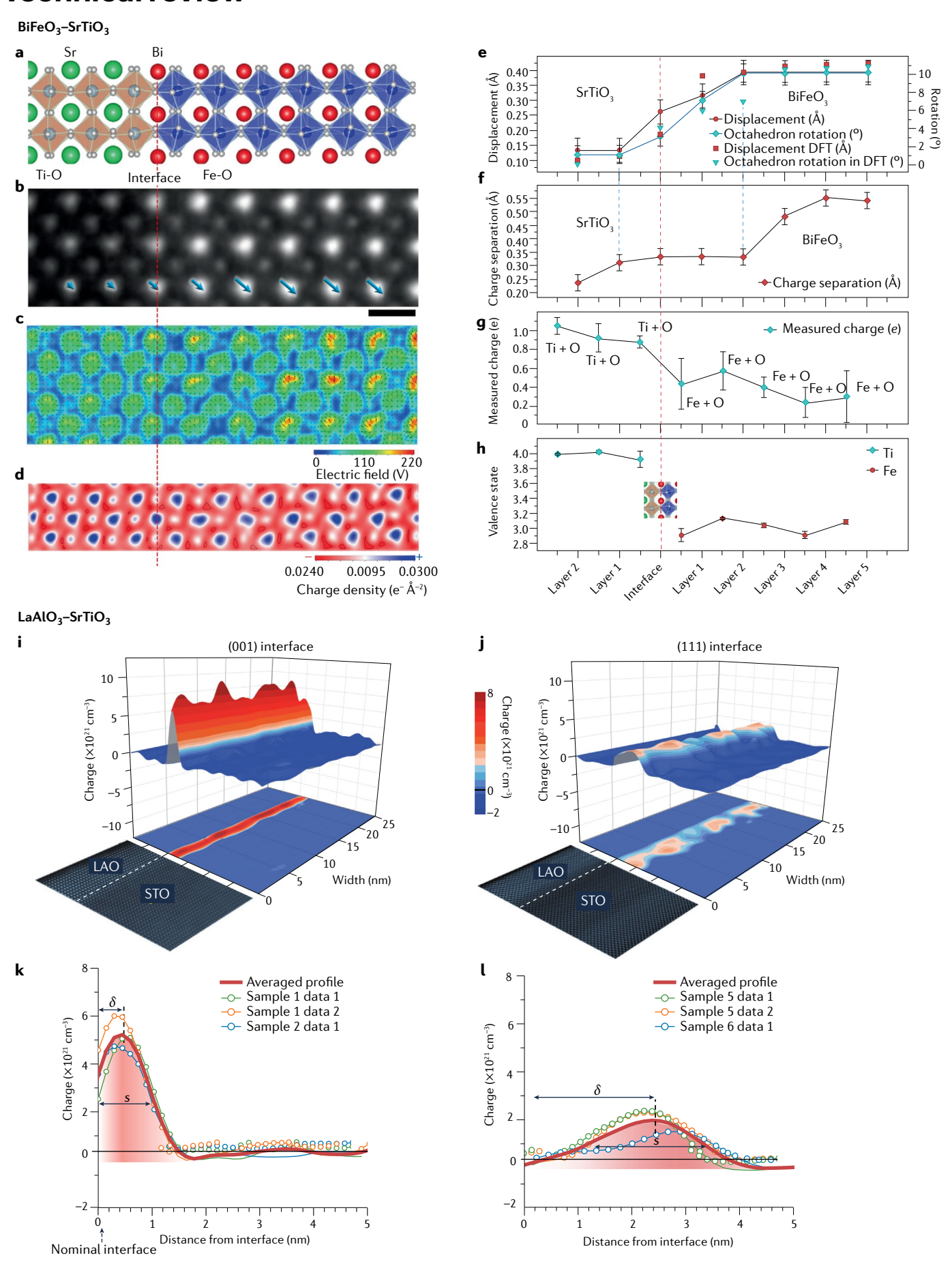


Fig. 6 | Applications to oxide interfaces. a, Atomic structure of the BiFeO₃-SrTiO₃ interface obtained from density functional theory (DFT) calculations. b, Atomic-resolution HAADF scanning transmission electron microscopy (STEM) image of the interface. Scale bar, 4 Å. The arrows indicate the direction and relative magnitude of Bi displacement. c,d, The corresponding electric field map (part c) and charge density image (part d) acquired by 4D-STEM. e, Changes in A-site (Sr or Bi) displacement (in Å) determined from part b and from DFT calculations. Error bars denote standard deviation. Also shown is the O octahedron rotation determined experimentally and from DFT calculations (in degrees). Error bars denote the detection limit. f, Separation between the weighted centres of positive and negative charges within each unit cell across the interface measured from part d. Error bars denote the detection limit. g, Total charge of Ti + O and Fe + O columns on each side of the interface measured from part d. Error bars denote the standard deviation. h, The valence state of Ti

and Fe measured using energy loss near edge structure. Error bars denote the standard deviation. The inset shows the position of the interface. ${\bf i}$, ${\bf j}$, 2D surface plot and projected map of the total charge density obtained by in-line electron holography for the LaAlO₃–SrTiO₃ (001) interface (part ${\bf i}$) and (111) interface (part ${\bf j}$), respectively. HAADF-STEM images are shown next to the charge density maps. ${\bf k}$, ${\bf j}$, 1D electron density obtained from the charge density maps of the (001) interface (part ${\bf k}$) and (111) interface (part ${\bf l}$). The solid red line corresponds to the average electron density from averaging three datasets. For the (001) interface, the density of the 2D electron gas (n_e) is $(2.88 \pm 0.39) \times 10^{14}$ cm⁻², which was calculated by integration of the averaged profile (region shaded red). The spatial depth (s) is 1.0 ± 0.3 nm and the maximum density (δ) is slightly displaced from the interface by about 0.4 nm. For the (111) interface, $n_e = (1.02 \pm 0.01) \times 10^{14}$ cm⁻², $s = 3.3 \pm 0.3$ and $\delta = 2.4$ nm. Panels ${\bf a} - {\bf h}$ adapted with permission from ref.⁷, Springer Nature Limited. Panels ${\bf i} - {\bf l}$ adapted from ref.¹⁰, Springer Nature Limited.

structures because of the low spatial resolution of the electron probe used in QCBED experiments and the requirement of periodicity in the QCBED analysis.

Similar capabilities have also been recently demonstrated in holography. In 2020, the charge of single sulfur monovacancies (V_s) was measured using off-axis holography¹¹ (Fig. 4i-k). In off-axis holography, the greatest challenge in reaching atomic-resolution charge density imaging has been the combined phase sensitivity and spatial resolution. Typically, phase sensitivity and spatial resolution are inversely proportional in holography, thus acquiring a dataset that has atomic resolution and phase sensitivity to detect weak shifts owing to the slight change in electron distribution is especially challenging. In this work, the high-resolution data were made possible by collecting a large series of holograms over several minutes followed by software-enabled correction of the mechanical drift from the sample stage and of the drift in the electronics controlling the biprism and wavefront/image-forming lenses. Such long total acquisition times are comparable to those in 4D-STEM; however, one advantage of holography is that the entire field of view is acquired in each frame, so that temporal resolution can be gained at the cost of increased noise—something that is generally not possible with commercially available 4D-STEM detectors. As noted in the paper¹¹, this makes holography better suited for observing dynamic processes in situ. However, segmented detectors can run at the same speed as conventional STEM detectors and, as mentioned previously. the frame times for the most advanced pixelated detectors are reaching the microsecond range⁵⁵⁻⁵⁸, which means that stacking multiple acquisitions¹¹¹ or observing dynamic phenomena will soon be possible in 4D-STEM as well.

Semiconductors

Initial studies⁵ of the charge density of individual atomic columns were conducted on semiconducting materials (Fig. 5a-e). In this study, quantitative charge density measurements from GaN collected with segmented detectors showed negative-charge pockets surrounding both Ga and N atomic columns. To demonstrate the influence of the nucleus and electrons separately, image simulations were performed in which the scattering potential of the positive and negative charges were separated and could each be included/excluded during the calculation. Only the simulation that included both the positive nuclear charge and the electron cloud reproduced the same charge density profile observed in the experiment, demonstrating that DPC/4D-STEM is sensitive to both the nuclear charge and the surrounding electron cloud.

Although high-resolution charge density imaging of individual atomic columns has been initiated using GaN as a model system, most studies of conventional semiconductor materials in which 4D-STEM is applied have focused on device applications in which the real-space distribution of the electric field and free charge determine the overall

functionality. In 2015, it was first demonstrated that DPC can detect the built-in electric field at a GaAs p-n junction 112. One of the key challenges in imaging the built-in electronic properties of doped semiconductor heterostructures is that the changes in the local field and charge caused by the dopants are relatively weak compared with that of atomic nuclei. Therefore, strategies must be devised to suppress the contributions of individual atomic columns. This study used a very large electron probe, with a spatial resolution of 12 nm, to average the field over a large area. However, using such a large probe will not always be feasible as devices continue to shrink in size. In 2021, another study⁸ improved on the earlier result by resolving nanoscale electric fields and electric potential changes also in a GaAs p-n junction. This improved approach used a standard high-resolution STEM probe (spatial resolution of <1 Å) and a sufficiently large step size that the atomic potential is randomly sampled. Combining this with a low-pass filter allows for the contributions of individual atoms to be eliminated, revealing the built-in field of the p-n junction with much higher spatial resolution.

Electron holography is a well-established technique for measuring electric potential, field and charge in semiconductor materials and devices. The technique was first demonstrated in 1999 $^{\! 113}$ and has seen wide applications in academia and industry^{114,115}. With lateral spatial resolution in the nanometer range, holography was the only method capable of mapping the embedded fields in semiconductor devices before the development of 4D-STEM. Mapping embedded fields is essential for measuring dopant distributions, which in turn determines the overall performance of the device. Subsequent studies have demonstrated phase sensitivity down to 0.1 V and spatial resolution down to 3 nm (refs. 116,117). In 2019, a study 118 directly compared holography and DPC for applications with semiconductor materials by imaging the same metal-oxide-semiconductor field effect transistor (MOSFET) and quantum well structures with both techniques (Fig. 5f-k). The paper concluded that both techniques can achieve similar spatial resolution and phase sensitivity, but not without some considerations. Holography is generally less affected by dynamic diffraction and is therefore more sensitive to weak fields than DPC. However, DPC can achieve a higher resolution while keeping the sample in the field of view because no reference wave is required (for the case of off-axis holography). However, these issues are both areas of active investigation. As discussed earlier, strategies for reducing the impact of dynamic diffraction are being developed for 4D-STEM/DPC; choosing an optimal probe size, step size or even using precession electron diffraction¹¹⁹ is a possible avenue. For holography, the development of in-line/ focal-series holography could eliminate the need for a reference wave at the cost of a more complex reconstruction process and less sensitivity to low-frequency information. However, recent advancements have improved the spatial resolution of in-line holography, such that it can also reach the full resolution achievable with off-axis holography¹²⁰.

Oxide heterostructures

Besides 2D materials, perovskite oxides have seen the most applications of DPC/4D-STEM in recent years. In perovskite oxides, like other strongly correlated materials, unexpected phenomena often emerge in interfaces, superlattices, domain walls or heterostructures 121-124. Often, multiple properties, such as lattice distortions, the local charge and chemistry, interact together to generate new phenomena in the heterostructure. The most prominent example of such emergent interfacial phenomenon is the 2D electron/hole gas (2DEG/2DHG) that has been discovered at the LaAlO₃-SrTiO₃ interface¹²⁵. Ferroelectric perovskite heterostructures and domain walls have also drawn significant attention because they can also form a 2DEG or 2DHG that is controllable with an external electric field 126-132. In all cases, the localized electronic properties occur within a few unit cells surrounding the interface, so TEM has had a large role in characterizing these material systems. Aberration-corrected STEM imaging and EELS are currently the primary TEM-based methods for understanding these heterostructures (see Box 1). However, recent advances in 4D-STEM and holography have enabled direct imaging of the electrostatic properties, which is complementary to the structural imaging and spectroscopic study.

4D-STEM electric field and charge density imaging have been applied to various oxide heterostructures and domain walls^{4,7,112,133}. The internal electric field of ferroelectric domains can generate contrast in DPC images⁴, and the polarization of ferroelectrics is reflected in the electric field of individual atomic columns, as shown in Ca-doped BiFeO₃ superlattices¹³³ and simulated BiFeO₃ structures¹³⁴. 4D-STEM for charge density imaging has been used to probe BiFeO₃ with a sub-ångström resolution⁷; a combination of atomic-resolution high angle annular dark-field (HAADF) imaging, 4D-STEM charge density imaging and first principles calculations has been applied to reveal the mechanism that leads to the emergence of a 2DEG at the interface (Fig. 6a–h). Three new methods were developed in this study for quantitatively measuring the oxygen octahedral tilt, the dipole of individual unit cells and the charge state of atomic columns using the charge density image and through a modification of Bader charge analysis^{135,136}.

These new methods helped to illustrate the asynchronous change in the atomic structure and charge distribution that leads to an accumulation of free charge, and the technique has been used to measure the charge state of a BiFeO $_3$ -TbScO $_3$ interface and directly image the polarization-controlled 2DEG/2DHG at the interface ¹³⁷. In a similar vein, atomic charge density imaging has been used to show how the conductivity of charged domain walls in BiFeO $_3$ can be attributed to an accumulation of oxygen vacancies; nanoscale charge density images showed an accumulation of charge at the domain wall, whereas

atomic-resolution charge density images revealed changes in the intensity of oxygen columns in charge density images, indicating the presence of oxygen vacancies ¹³⁸. Atomic-resolution charge density imaging has also been used to show the charge transfer between an oxide support and a gold nanoparticle catalyst. Direct visualization of the charge transfer with 4D-STEM revealed how oxygen treatment of the heterogeneous catalyst can switch the sign of the charge accumulated at the surface of the oxide support ¹³⁹.

Nanoscale 4D-STEM electric field and polarization mapping have also had an important role in characterizing the electronic properties of the recently discovered polar vortex¹⁴⁰ and skyrmion¹⁴¹ nanodomains found in PbTiO₃-SrTiO₃ superlattices and multilayer systems. In both cases, simultaneous mapping of the electric field and ferroelectric polarization using 4D-STEM data enabled the discovery of stable regions of localized negative capacitance^{50,142}. A similar polarization mapping technique has also been used to image the skyrmion-like nanodomains found in a freestanding PbTiO₃-SrTiO₃ bilayer film⁵¹. In contrast to most of the other research discussed here, the 4D-STEM data in these studies were collected with a low convergence angle, so that the CBED discs were well separated, instead of overlapping. While this reduces the spatial resolution of the probe, it also allows for the electric field and polarization to be simultaneously calculated from the central and outer diffraction discs in the same dataset 49,53,143, respectively. This enables the calculation of further electronic properties such as the local capacitance.

Electron holography has also been recently applied to oxide interfaces. The geometry of samples with buried interfaces lends themselves more towards in-line holography because a vacuum region does not need to be included in the field of view to provide a reference wave. Fullresolution in-line holography¹²⁰ has been applied to an LaAlO₃-SrTiO₃ interface to study the differences in (001) and (111) oriented interfaces¹⁰ (Fig. 6i-l). In in-line holography, multiple images are collected with a known change in defocus between each image; this enables an iterative reconstruction of the exit wave phase. The study showed that the 2DEG at the (001) interface is concentrated within 1 nm of the interface on the SrTiO₂ side, whereas the 2DEG at the (111) interface is spread between 1 and 4 nm from the interface on the SrTiO₃ side. This was attributed to the differences in relative orientation of the interface and d orbitals. which the accumulated electrons occupy. An in-depth analysis of the differences between off-axis, in-line and hybrid holography using the LaAlO₃-SrTiO₃ (111) interface as a model system can be found in ref. 144. In hybrid holography, the data from off-axis holography are used as an initial guess for the iterative reconstruction by in-line holography of the same region^{145,146}. Although the known deficiencies of off-axis

Table 1 | Technical details of methods in electron microscopy

| Technique | Charge density image | Sample requirements | Specialized microscopic hardware | Computational difficulty |
|--|---|---|--|---|
| Quantitative convergent beam electron diffraction | Full 3D distribution based on fitting with simulated structure factors | Thick enough for dynamic diffraction to be clearly visible (t>30nm) | Energy filter | High, simulation and fitting process is complex and time-consuming |
| 4D scanning transmission electron microscopy | 2D projection based on shift in probe momentum | Thin enough for phase-object approximation for highest spatial resolution (t<6nm) | Fast camera synchronized to scanning coils | Medium, datasets can grow very large (10–100 GB) |
| Holography | 2D projection based on interference pattern or iterative reconstruction | Thin enough for phase-object approximation for highest spatial resolution (t<6nm) | Bi-prism (off-axis holography) | Low (off-axis holography) Medium (in-line holography requires iterative reconstruction) |

and in-line holography in reconstructing high-frequency and low-frequency information, respectively, were translated to the detection of the 2DEG, hybrid holography could reconstruct the full frequency range faithfully. Beyond the LaAlO₃–SrTiO₃ interface, off-axis holography has also been applied to visualize the effects of charge transfer caused by band bending at a Pt–TiO₂ interface 147 .

Outlook

Among the electron microscopy techniques for imaging the real-space charge distribution and other associated electrostatic properties in materials, QCBED can determine the charge density with high precision in three dimensions for homogeneous materials; 4D-STEM and holography measure the landscape of electrostatic potential by following the phase-object approximation (in the kinematic diffraction regime). Although limited by the fact that the mapped charge distribution is the projection in two dimensions, 4D-STEM and holography can be more easily applied to nanostructures and heterogeneous materials because of both the higher spatial resolution and the less restrictive boundary conditions necessary to complete the data analysis. A summary of the capabilities and requirements of these techniques is presented in Table 1.

Note that the limitation of using phase retrieval methods in electron microscopy to map local charge at the atomic scale is obvious. The phase change is approximated to be linear to the local potential; however, the interaction of the electron probe with sample is usually more complicated. In addition to the effects of dynamic scattering, residual aberrations can also influence the relationship between the phase of the electron beam and the local potential. In holography, uncorrected aberrations affect the quality of the final phase image, and in 4D-STEM, they limit the size of the electron probe. Although the electron probe size is already smaller than that of an atom, positive charges from the nuclei still strongly contribute to the Coulomb force felt by the electron probe, and the changes of the internal electrostatic potential between atoms can also occur at even smaller length scales than the probe size. Therefore, the charge density image acquired in 4D-STEM is generally regarded as a convolution of the true charge density with intensity distribution of the electron probe and often requires additional modelling to accurately interpret.

Moving forward, algorithmic improvements to consider the non-linearity in the potential-phase relation 148, technique advancement in data acquisition and processing, including the incorporation of machine learning methods 149, sample preparation, and perhaps more importantly, improvements in aberration correction, stability and other features offered by newly developed instruments, all can improve the feasibility and reliability in characterizing the charge distribution and other electromagnetic properties in materials. For example, the intrinsic magnetic field of an anti-ferromagnetic material was recently visualized at the atomic scale through combined innovations in microscopy hardware and advanced image filtering techniques 150.

Finally, as briefly mentioned earlier, microscopic properties are often directly influenced by microscale or even atomic-scale electronic structure, but linking knowledge gained between vastly different length scales often remains challenging. 4D-STEM and electron microscopy, in general, are now the ideal tool to resolve the structure-property relationship across different length scales, because by simply changing the convergence angles, the size of the electron probe can vary from sub-ångström to tens of nanometres, covering at least three orders of magnitude in size, easily matching the dimension of the features and properties of interest. Connecting atomic-scale field

and charge distributions to microscale and larger-scale properties is thus possible ^{139,151,152}.

Published online: 9 December 2022

References

- . Genoni, A. et al. Quantum crystallography: current developments and future perspectives. *Chem. A Eur. J.* **24**, 10881–10905 (2018).
- Nakashima Philip, N. H., Smith Andrew, E., Etheridge, J. & Muddle Barrington, C. The bonding electron density in aluminum. Science 331, 1583–1586 (2011).
- Peng, D. & Nakashima, P. N. H. Measuring density functional parameters from electron diffraction patterns. *Phys. Rev. Lett.* 126, 176402 (2021).
- Shibata, N. et al. Differential phase-contrast microscopy at atomic resolution. Nat. Phys. 8, 611–615 (2012)
- Sánchez-Santolino, G. et al. Probing the internal atomic charge density distributions in real space. ACS Nano 12, 8875–8881 (2018).
- Müller, K. et al. Atomic electric fields revealed by a quantum mechanical approach to electron picodiffraction. Nat. Commun. 5, 5653 (2014).
- Gao, W. et al. Real-space charge-density imaging with sub-ångström resolution by four-dimensional electron microscopy. Nature 575, 480–484 (2019).
- Beyer, A. et al. Quantitative characterization of nanometer-scale electric fields via momentum-resolved STEM. Nano Lett. 21, 2018–2025 (2021).
- Zheng, Q. et al. Direct visualization of anionic electrons in an electride reveals inhomogeneities. Sci. Adv. 7, eabe6819 (2021).
- Song, K. et al. Direct imaging of the electron liquid at oxide interfaces. Nat. Nanotechnol. 13, 198–203 (2018).
- Boureau, V. et al. Quantitative mapping of the charge density in a monolayer of MoS₂ at atomic resolution by off-axis electron holography. ACS Nano 14, 524–530 (2020).
- Winkler, F. et al. Absolute scale quantitative off-axis electron holography at atomic resolution. Phys. Rev. Lett. 120, 156101 (2018).
- Massa, L., Huang, L. & Karle, J. Quantum crystallography and the use of kernel projector matrices. Int. J. Quantum Chem. 56, 371–384 (1995).
- 14. Piela, L. Ideas of Quantum Chemistry (Elsevier, 2014).
- 15. Johnson, K. H. Quantum chemistry. Annu. Rev. Phys. Chem. 26, 39-57 (1975).
- Helgaker, T., Klopper, W. & Tew, D. P. Quantitative quantum chemistry. Mol. Phys. 106, 2107–2143 (2008).
- Hansen, N. K. & Coppens, P. Testing aspherical atom refinements on small-molecule data sets. Acta Crystallogr. A 34, 909–921 (1978).
- Stewart, R. Electron population analysis with rigid pseudoatoms. Acta Crystallogr. A 32, 565–574 (1976).
- Fischer, A. et al. Experimental and theoretical charge density studies at subatomic resolution. J. Phys. Chem. A 115, 13061–13071 (2011).
- Makal, A. M., Plażuk, D., Zakrzewski, J., Misterkiewicz, B. & Woźniak, K. Experimental charge density analysis of symmetrically substituted ferrocene derivatives. *Inorg. Chem.* 49, 4046–4059 (2010).
- Dittrich, B., Sze, E., Holstein, J. J., Hubschle, C. B. & Jayatilaka, D. Crystal-field effects in L-homoserine: multipoles versus quantum chemistry. Acta Crystallogr. A 68, 435–442 (2012).
- Metherell, J. F. in Electron Microscopy in Materials Science, Part 2 Vol. 397 (eds Valdre, U. & Ruedl, E.) 401–550 (1976).
- Midgley Paul, A. Electronic bonding revealed by electron diffraction. Science 331, 1528–1529 (2011).
- 24. Zuo, J. M. & Spence, J. C. H. Electron Microdiffraction (Springer, 1991)
- Tsuda, K. & Tanaka, M. Refinement of crystal structure parameters using convergentbeam electron diffraction: the low-temperature phase of SrTiO3. Acta Crystallogr. A 51, 7-19 (1995).
- Zuo, J. M., Kim, M., O'Keeffe, M. & Spence, J. C. H. Direct observation of d-orbital holes and Cu–Cu bonding in Cu2O. Nature 401, 49–52 (1999).
- Koshima, H. Photomechanical motion of molecular crystals. Acta Crystallogr. A 67, C176 (2011).
- Sang, X. H., Kulovits, A. & Wiezorek, J. M. K. Simultaneous determination of highly precise Debye-Waller factors and structure factors for chemically ordered NiAl. Acta Crystallogr. A 66, 694-702 (2010).
- Jiang, B., Zuo, J. M., Jiang, N., O'Keeffe, M. & Spence, J. C. Charge density and chemical bonding in rutile, TiO2. Acta Crystallogr. A 59, 341–350 (2003).
- Pennington, R. S., Wang, F. & Koch, C. T. Stacked-Bloch-wave electron diffraction simulations using GPU acceleration. *Ultramicroscopy* 141, 32–37 (2014).
- Cowley, J. M. & Moodie, A. F. The scattering of electrons by atoms and crystals. I. A new theoretical approach. Acta Crystallogr. 10, 609–619 (1957).
- Saunders, M. et al. Measurement of low-order structure factors for silicon from zone-axis CBED patterns. Ultramicroscopy 60, 311–323 (1995).
- Müller, K. et al. Refinement of the 200 structure factor for GaAs using parallel and convergent beam electron nanodiffraction data. *Ultramicroscopy* 109, 802–814 (2009).
- Ogata, Y., Tsuda, K., Akishige, Y. & Tanaka, M. Refinement of the crystal structural parameters of the intermediate phase of h-BaTiO3 using convergent-beam electron diffraction. Acta Crystallogr. A 60, 525-531 (2004).
- Ogata, Y., Tsuda, K. & Tanaka, M. Determination of the electrostatic potential and electron density of silicon using convergent-beam electron diffraction. Acta Crystallogr. A 64, 587-597 (2008).

- Nakashima, P. N. H. Quantitative convergent-beam electron diffraction and quantum crystallography — the metallic bond in aluminium. Struct. Chem. 28, 1319–1332 (2017).
- Zuo, J. M. Measurements of electron densities in solids: a real-space view of electronic structure and bonding in inorganic crystals. Rep. Prog. Phys. 67, 2053–2103 (2004).
- Tanaka, M. & Tsuda, K. Convergent-beam electron diffraction. J. Electron. Microsc. 60, S245–S267 (2011).
- Vulović, M., Voortman, L. M., van Vliet, L. J. & Rieger, B. When to use the projection assumption and the weak-phase object approximation in phase contrast cryo-EM. Ultramicroscopy 136, 61–66 (2014).
- 40. Kirkland, E. J. Advanced Computing in Electron Microscopy 3rd edn (Springer, 2020).
- Knut, M. in Transmissionelektronenmikroskopie von InGaNAs Nanostrukturen mittels ab-initio Strukturfaktoren für verspannungsrelaxierte Superzellen (Universität Bremen FB1 Physik/Flektrotechnik. 2011).
- 42. Brown, H. G. Advances in Atomic Resolution Imaging Using Scanning Transmission Flectron Microscopy (2017)
- Winkler, F., Barthel, J., Dunin-Borkowski, R. E. & Müller-Caspary, K. Direct measurement of electrostatic potentials at the atomic scale: a conceptual comparison between electron holography and scanning transmission electron microscopy. *Ultramicroscopy* 210, 112926 (2020).
- Hachtel, J. A., Idrobo, J. C. & Chi, M. Sub-ångstrom electric field measurements on a universal detector in a scanning transmission electron microscope. Adv. Struct. Chem. Imaging 4, 10 (2018).
- Shukla, A. K. et al. Effect of composition on the structure of lithium- and manganese-rich transition metal oxides. Energy Environ. Sci. 11, 830–840 (2018).
- Nalin Mehta, A. et al. Unravelling stacking order in epitaxial bilayer MX2 using 4D-STEM with unsupervised learning. Nanotechnology 31, 445702 (2020).
- Ozdol, V. B. et al. Strain mapping at nanometer resolution using advanced nano-beam electron diffraction. Appl. Phys. Lett. 106, 253107 (2015).
- LeBeau, J. M., Findlay, S. D., Allen, L. J. & Stemmer, S. Position averaged convergent beam electron diffraction: theory and applications. *Ultramicroscopy* 110, 118–125 (2010).
- Tsuda, K., Yasuhara, A. & Tanaka, M. Two-dimensional mapping of polarizations of rhombohedral nanostructures in the tetragonal phase of BaTiO₃ by the combined use of the scanning transmission electron microscopy and convergent-beam electron diffraction methods. Appl. Phys. Lett. 103, 082908 (2013).
- Yadav, A. K. et al. Spatially resolved steady-state negative capacitance. Nature 565, 468–471 (2019).
- Han, L. et al. High-density switchable skyrmion-like polar nanodomains integrated on silicon. Nature 603, 63–67 (2022).
- Panova, O. et al. Diffraction imaging of nanocrystalline structures in organic semiconductor molecular thin films. Nat. Mater. 18, 860–865 (2019).
- Cao, M. C. et al. Theory and practice of electron diffraction from single atoms and extended objects using an EMPAD. *Microscopy* 67, i150–i161 (2018).
- 54. Levin, B. D. A. Direct detectors and their applications in electron microscopy for materials science. *J. Phys. Mater.* **4**, 042005 (2021).
- Plotkin-Swing, B. et al. 100,000 Diffraction patterns per second with live processing for 4D-STEM. Microsc. Microanal. 28, 422–424 (2022).
- Ciston, J. et al. The 4D camera: very high speed electron counting for 4D-STEM. Microsc. Microanal. 25, 1930–1931 (2019).
- Microanal. 25, 1930–1931 (2019).
 Ercius, P. et al. The 4D camera an 87 kHz frame-rate detector for counted 4D-STEM experiments. Microsc. Microanal. 26, 1896–1897 (2020).
- Philipp, H. et al. Wide dynamic range, 10 kHz framing detector for 4D-STEM. Microsc. Microanal. 27, 992–993 (2021).
- Ophus, C. Four-dimensional scanning transmission electron microscopy (4D-STEM): from scanning nanodiffraction to ptychography and beyond. *Microsc. Microanal.* 25, 563–582 (2019).
- MacLaren, I., Macgregor, T. A., Allen, C. S. & Kirkland, A. I. Detectors the ongoing revolution in scanning transmission electron microscopy and why this important to material characterization. APL Mater. 8, 110901 (2020).
- Rose, H. Phase contrast in scanning transmission electron microscopy. Optik 39, 416–436 (1974).
- 62. De Christoph, H. Differential phase constrast in a STEM. Optik 41, 452-456 (1974).
- Rose, H. Nonstandard imaging methods in electron microscopy. Ultramicroscopy 2, 251–267 (1976).
- Lazić, I., Bosch, E. G. T. & Lazar, S. Phase contrast STEM for thin samples: integrated differential phase contrast. *Ultramicroscopy* 160, 265–280 (2016).
- Close, R., Chen, Z., Shibata, N. & Findlay, S. D. Towards quantitative, atomic-resolution reconstruction of the electrostatic potential via differential phase contrast using electrons. *Ultramicroscopy* 159, 124–137 (2015).
- Brown, H. G. et al. Measuring nanometre-scale electric fields in scanning transmission electron microscopy using segmented detectors. *Ultramicroscopy* 182, 169–178 (2017).
- 67. Gabor, D. A new microscopic principle. Nature 161, 777-778 (1948).
- Gabor, D. & Bragg, W. L. Microscopy by reconstructed wave-fronts. Proc. R. Soc. Lond. Ser. A Math. Phys. Sci. 197, 454–487 (1949).
- Lichte, H. & Lehmann, M. Electron holography basics and applications. Rep. Prog. Phys 71, 016102 (2007).
- Linck, M., Freitag, B., Kujawa, S., Lehmann, M. & Niermann, T. State of the art in atomic resolution off-axis electron holography. *Ultramicroscopy* 116, 13–23 (2012).
- Bürger, J., Riedl, T. & Lindner, J. K. N. Influence of lens aberrations, specimen thickness and tilt on differential phase contrast STEM images. *Ultramicroscopy* 219, 113118 (2020).

- Lichte, H. Performance limits of electron holography. *Ultramicroscopy* 108, 256–262 (2008).
- Müller-Caspary, K. et al. Measurement of atomic electric fields and charge densities from average momentum transfers using scanning transmission electron microscopy. *Ultramicroscopy* 178, 62–80 (2017).
- Addiego, C., Gao, W. & Pan, X. Thickness and defocus dependence of inter-atomic electric fields measured by scanning diffraction. *Ultramicroscopy* 208, 112850 (2020)
- Robert, H. L. et al. Dynamical diffraction of high-energy electrons investigated by focal series momentum-resolved scanning transmission electron microscopy at atomic resolution. *Ultramicroscopy* 233, 113425 (2022).
- Lehmann, M. Determination and correction of the coherent wave aberration from a single off-axis electron hologram by means of a genetic algorithm. *Ultramicroscopy* 85, 165–182 (2000).
- Rodenburg, J. M. in Advances in Imaging and Electron Physics Vol. 150 (ed. Hawkes, P.) 87-184 (Flsevier. 2008).
- Rodenburg, J. M. & Faulkner, H. M. L. A phase retrieval algorithm for shifting illumination. Appl. Phys. Lett. 85, 4795–4797 (2004).
- Maiden, A. M. & Rodenburg, J. M. An improved ptychographical phase retrieval algorithm for diffractive imaging. *Ultramicroscopy* 109, 1256–1262 (2009).
- Rodenburg, J. M. & Bates, R. H. T. The theory of super-resolution electron microscopy via Wigner-distribution deconvolution. *Philos. Trans. R. Soc. Lond. Ser. A Phys. Eng. Sci.* 339, 521–553 (1992).
- Nellist, P. D., McCallum, B. C. & Rodenburg, J. M. Resolution beyond the 'information limit' in transmission electron microscopy. *Nature* 374, 630–632 (1995).
- Maiden, A. M., Humphry, M. J. & Rodenburg, J. M. Ptychographic transmission microscopy in three dimensions using a multi-slice approach. J. Opt. Soc. Am. A 29, 1606–1614 (2012)
- Wang, P., Zhang, F., Gao, S., Zhang, M. & Kirkland, A. I. Electron ptychographic diffractive imaging of boron atoms in LaB6 crystals. Sci. Rep. 7, 2857 (2017).
- Zhou, L. et al. Low-dose phase retrieval of biological specimens using cryo-electron ptychography. Nat. Commun. 11, 2773 (2020).
- Yang, H. et al. Electron ptychographic phase imaging of light elements in crystalline materials using Wigner distribution deconvolution. *Ultramicroscopy* 180, 173–179 (2017)
- Pennycook, T. J. et al. Efficient phase contrast imaging in STEM using a pixelated detector. Part 1: experimental demonstration at atomic resolution. *Ultramicroscopy* 151, 160–167 (2015).
- Yang, H. et al. Simultaneous atomic-resolution electron ptychography and Z-contrast imaging of light and heavy elements in complex nanostructures. Nat. Commun. 7, 12532 (2016)
- Lozano, J. G., Martinez, G. T., Jin, L., Nellist, P. D. & Bruce, P. G. Low-dose aberrationfree imaging of Li-rich cathode materials at various states of charge using electron ptychography. Nano Lett. 18, 6850–6855 (2018).
- Chen, Z. et al. Mixed-state electron ptychography enables sub-ångström resolution imaging with picometer precision at low dose. *Nat. Commun.* 11, 2994 (2020).
- Gao, S. et al. Electron ptychographic microscopy for three-dimensional imaging Nat. Commun. 8. 163 (2017).
- Jiang, Y. et al. Electron ptychography of 2D materials to deep sub-ångström resolution. Nature 559, 343–349 (2018).
- 92. Chen, Z. et al. Electron ptychography achieves atomic-resolution limits set by lattice vibrations. Science **372**, 826–831 (2021).
- Martinez, G. T. et al. Direct imaging of charge redistribution due to bonding at atomic resolution via electron ptychography. Preprint at https://doi.org/10.48550/ arXiv.1907.12974 (2019).
- Lupini, A. R., Oxley, M. P. & Kalinin, S. V. Pushing the limits of electron ptychography. Science 362, 399–400 (2018).
- Rodenburg, J. & Maiden, A. in Springer Handbook of Microscopy (eds Hawkes, P. W. & Spence, J. C. H.) 819–904 (Springer, 2019).
- Ge, R. et al. Atomristor: nonvolatile resistance switching in atomic sheets of transition metal dichalcogenides. Nano Lett. 18, 434–441 (2018).
- Kim, M. et al. Zero-static power radio-frequency switches based on MoS₂ atomristors. Nat. Commun. 9, 2524 (2018).
- Akinwande, D., Petrone, N. & Hone, J. Two-dimensional flexible nanoelectronics. Nat. Commun. 5, 5678 (2014).
- Siao, M. D. et al. Two-dimensional electronic transport and surface electron accumulation in MoS₂. Nat. Commun. 9, 1442 (2018).
- 100. Geim, A. K. Graphene: status and prospects. Science 324, 1530-1534 (2009).
- Castro Neto, A. H., Guinea, F., Peres, N. M. R., Novoselov, K. S. & Geim, A. K. The electronic properties of graphene. Rev. Mod. Phys. 81, 109–162 (2009).
- Banhart, F., Kotakoski, J. & Krasheninnikov, A. V. Structural defects in graphene. ACS Nano 5, 26–41 (2011).
- Wang, L. et al. Fundamental transport mechanisms, fabrication and potential applications of nanoporous atomically thin membranes. *Nat. Nanotechnol.* 12, 509–522 (2017).
- 104. Fang, S. et al. Atomic electrostatic maps of 1D channels in 2D semiconductors using 4D scanning transmission electron microscopy. Nat. Commun. 10, 1127 (2019).
- Han, Y. et al. Sub-nanometre channels embedded in two-dimensional materials. Nat. Mater. 17, 129–133 (2018).

- Huang, L. et al. Anomalous fracture in two-dimensional rhenium disulfide. Sci. Adv. 6, eabc2282 (2020).
- O'Leary, C. M. et al. Phase reconstruction using fast binary 4D STEM data. Appl. Phys. Lett. 116, 124101 (2020).
- Chang, S. L. Y., Dwyer, C., Barthel, J., Boothroyd, C. B. & Dunin-Borkowski, R. E. Performance of a direct detection camera for off-axis electron holography. *Ultramicroscopy* 161, 90–97 (2016).
- Müller-Caspary, K. et al. Atomic-scale quantification of charge densities in two-dimensional materials. Phys. Rev. B 98, 121408 (2018).
- Ishikawa, R. et al. Direct electric field imaging of graphene defects. Nat. Commun. 9, 3878 (2018).
- O'Leary, C. M., Haas, B., Koch, C. T., Nellist, P. D. & Jones, L. Increasing spatial fidelity and SNR of 4D-STEM using multi-frame data fusion. *Microsc. Microanal.* 28, 1417–1427 (2022).
- Shibata, N. et al. Imaging of built-in electric field at a p-n junction by scanning transmission electron microscopy. Sci. Rep. 5, 10040 (2015).
- Rau, W. D., Schwander, P., Baumann, F. H., Höppner, W. & Ourmazd, A. Two-dimensional mapping of the electrostatic potential in transistors by electron holography. *Phys. Rev. Lett.* 82, 2614–2617 (1999).
- McCartney, M. R. & Smith, D. J. Electron holography: phase imaging with nanometer resolution. *Annu. Rev. Mater. Res.* 37, 729–767 (2007).
- McCartney, M. R., Dunin-Borkowski, R. E. & Smith, D. J. Quantitative measurement of nanoscale electrostatic potentials and charges using off-axis electron holography: developments and opportunities. *Ultramicroscopy* 203, 105–118 (2019).
- Han, M.-G. et al. Sample preparation for precise and quantitative electron holographic analysis of semiconductor devices. *Microsc. Microanal.* 12, 295–301 (2006).
- 117. Ikarashi, N., Takeda, H., Yako, K. & Hane, M. In-situ electron holography of surface potential response to gate voltage application in a sub-30-nm gate-length metal-oxide-semiconductor field-effect transistor. Appl. Phys. Lett. 100, 143508 (2012).
- Haas, B., Rouvière, J.-L., Boureau, V., Berthier, R. & Cooper, D. Direct comparison of off-axis holography and differential phase contrast for the mapping of electric fields in semiconductors by transmission electron microscopy. *Ultramicroscopy* 198, 58–72 (2019)
- Bruas, L. et al. Improved measurement of electric fields by nanobeam precession electron diffraction. J. Appl. Phys. 127, 205703 (2020).
- 120. Koch, C. T. Towards full-resolution inline electron holography. Micron 63, 69-75 (2014).
- Schlom, D. G. et al. Elastic strain engineering of ferroic oxides. MRS Bull. 39, 118–130 (2014).
- 122. Huyan, H., Li, L., Addiego, C., Gao, W. & Pan, X. Structures and electronic properties of domain walls in BiFeO₃ thin films. *Natl Sci. Rev.* **6**, 669–683 (2019).
- Ye, F. et al. Emergent properties at oxide interfaces controlled by ferroelectric polarization. npi Comput. Mater. 7. 130 (2021).
- 124. Ramesh, R. & Schlom, D. G. Creating emergent phenomena in oxide superlattices. Nat. Rev. Mater. 4, 257–268 (2019).
- Ohtomo, A. & Hwang, H. Y. A high-mobility electron gas at the LaAlO₃/SrTiO₃ heterointerface. Nature 427, 423–426 (2004).
- Niranjan, M. K., Wang, Y., Jaswal, S. S. & Tsymbal, E. Y. Prediction of a switchable twodimensional electron gas at ferroelectric oxide interfaces. *Phys. Rev. Lett.* 103, 016804 (2009).
- Zhang, Z., Wu, P., Chen, L. & Wang, J. First-principles prediction of a two dimensional electron gas at the BiFeO3/SrTiO3 interface. Appl. Phys. Lett. 99, 062902 (2011).
- Fredrickson, K. D. & Demkov, A. A. Switchable conductivity at the ferroelectric interface: nonpolar oxides. Phys. Rev. B 91, 115126 (2015).
- 129. Yin, B., Aguado-Puente, P., Qu, S. & Artacho, E. Two-dimensional electron gas at the PbTiO₃/SrTiO₃ interface: an ab initio study. *Phys. Rev. B* 92, 115406 (2015).
- Zhang, Y. et al. Anisotropic polarization-induced conductance at a ferroelectric-insulator interface. Nat. Nanotechnol. 13, 1132–1136 (2018).
- Li, L. et al. Giant resistive switching via control of ferroelectric charged domain walls.
 Adv. Mater. 28, 6574-6580 (2016).
 Ma, J. et al. Controllable conductive readout in self-assembled, topologically confined
- ferroelectric domain walls. *Nat. Nanotechnol.* **13**, 947–952 (2018).
- Campanini, M., Erni, R., Yang, C. H., Ramesh, R. & Rossell, M. D. Periodic giant polarization gradients in doped BiFeO3 thin films. Nano Lett. 18, 717–724 (2018).
- Campanini, M. et al. Atomic-resolution differential phase contrast STEM on ferroelectric materials: a mean-field approach. *Phys. Rev. B* 101, 184116 (2020).
- Bader, R. F. W. & Nguyen-Dang, T. T. in Advances in Quantum Chemistry Vol. 14 (ed. Löwdin, P.-O.) 63–124 (Academic Press, 1981).
- Henkelman, G., Arnaldsson, A. & Jónsson, H. A fast and robust algorithm for Bader decomposition of charge density. Comput. Mater. Sci. 36, 354–360 (2006).
- Huyan, H. et al. Direct observation of polarization-induced two-dimensional electron/ hole gases at ferroelectric-insulator interface. npi Quantum Mater. 6, 88 (2021).
- Campanini, M. et al. Imaging and quantification of charged domain walls in BiFeO₃. Nanoscale 12, 9186–9193 (2020).
- Zachman, M. J. et al. Measuring and directing charge transfer in heterogenous catalysts. Nat. Commun. 13, 3253 (2022).
- Yadav, A. K. et al. Observation of polar vortices in oxide superlattices. *Nature* 530, 198–201 (2016).
- Das, S. et al. Observation of room-temperature polar skyrmions. Nature 568, 368–372 (2019).

- Das, S. et al. Local negative permittivity and topological phase transition in polar skyrmions. Nat. Mater. 20, 194–201 (2021).
- Deb, P. et al. Imaging polarity in two dimensional materials by breaking Friedel's Law. Ultramicroscopy 215, 113019 (2020).
- Seo, J., Koch, C. T., Ryu, S., Eom, C.-B. & Oh, S. H. Analysis of local charges at heterointerfaces by electron holography—a comparative study of different techniques. *Ultramicroscopy* 231, 113236 (2021).
- 145. Ozsoy-Keskinbora, C., Boothroyd, C. B., Dunin-Borkowski, R. E., van Aken, P. A. & Koch, C. T. Hybridization approach to in-line and off-axis (electron) holography for superior resolution and phase sensitivity. Sci. Rep. 4, 7020 (2014).
- Ozsoy-Keskinbora, C., Boothroyd, C. B., Dunin-Borkowski, R. E., van Aken, P. A.
 Koch, C. T. Mapping the electrostatic potential of Au nanoparticles using hybrid electron holography. *Ultramicroscopy* 165, 8-14 (2016).
- Nakajima, H. et al. Electrostatic potential measurement at the Pt/TiO₂ interface using electron holography. J. Appl. Phys. 129, 174304 (2021).
- Wu, L., Meng, Q. & Zhu, Y. Mapping valence electron distributions with multipole density formalism using 4D-STEM. Ultramicroscopy 219, 113095 (2020).
- Zhang, C., Han, R., Zhang, A. R. & Voyles, P. M. Denoising atomic resolution 4D scanning transmission electron microscopy data with tensor singular value decomposition. *Ultramicroscopy* 219, 113123 (2020).
- Kohno, Y., Seki, T., Findlay, S. D., Ikuhara, Y. & Shibata, N. Real-space visualization of intrinsic magnetic fields of an antiferromagnet. *Nature* 602, 234–239 (2022).
- 151. Addiego, C., Gao, W. & Pan, X. Multiscale electric field imaging of vortices in PbTiO₃-SrTiO₃ superlattice. *Microsc. Microanal.* 26, 466–468 (2020).
- 152. Eldred, T. B., Smith, J. G. & Gao, W. Polarization fluctuation of BaTiO₃ at unit cell level mapped by four-dimensional scanning transmission electron microscopy. J. Vac. Sci. Technol. A 40, 013205 (2021).
- Tan, H., Verbeeck, J., Abakumov, A. & Van Tendeloo, G. Oxidation state and chemical shift investigation in transition metal oxides by EELS. *Ultramicroscopy* 116, 24–33 (2012).
- 154. Zhang, Z., Sigle, W. & Rühle, M. Atomic and electronic characterization of the a[100] dislocation core in SrTiO₃. Phys. Rev. B 66, 094108 (2002).
- Egerton, R. Electron Energy-Loss Spectroscopy in the Electron Microscope 3rd edn (Springer, 2011).
- Muller, D. A. Simple model for relating EELS and XAS spectra of metals to changes in cohesive energy. Phys. Rev. B 58, 5989–5995 (1998).
- Hitchcock, A. P. Near edge electron energy loss spectroscopy: comparison to X-ray absorption. Jpn J. Appl. Phys. 32, 176 (1993).
- Mory, C., Kohl, H., Tencé, M. & Colliex, C. Experimental investigation of the ultimate EELS spatial resolution. *Ultramicroscopy* 37, 191–201 (1991).
- Hitchcock, A. P., Dynes, J. J., Johansson, G., Wang, J. & Botton, G. Comparison of NEXAFS microscopy and TEM-EELS for studies of soft matter. *Micron* 39, 741–748 (2008).
- Wang, Z. L., Yin, J. S. & Jiang, Y. D. EELS analysis of cation valence states and oxygen vacancies in magnetic oxides. *Micron* 31, 571–580 (2000).
- Rez, P. & Muller, D. A. The theory and interpretation of electron energy loss near-edge fine structure. *Annu. Rev. Mater. Res.* 38, 535–558 (2008).
- 162. Colella, M., Lumpkin, G. R., Zhang, Z., Buck, E. C. & Smith, K. L. Determination of the uranium valence state in the brannerite structure using EELS, XPS, and EDX. Phys. Chem. Miner. 32, 52–64 (2005).
- 163. Yoshiya, M., Tanaka, I., Kaneko, K. & Adachi, H. First principles calculation of chemical shifts in ELNES/NEXAFS of titanium oxides. J. Phys. Condens. Matter 11, 3217–3228 (1999).
- Lee, J. S. et al. Titanium d_{xy} ferromagnetism at the LaAlO₃/SrTiO₃ interface. *Nat. Mater.* 12, 703–706 (2013).
- 165. Ma, C. et al. Atomic-scale origin of the large grain-boundary resistance in perovskite Li-ion-conducting solid electrolytes. *Energy Environ. Sci.* **7**, 1638–1642 (2014).
- 166. Yu, L., Li, M., Wen, J., Amine, K. & Lu, J. (S)TEM-EELS as an advanced characterization technique for lithium-ion batteries. Mater. Chem. Front. 5, 5186–5193 (2021).
- 167. Su, L. et al. Direct observation of elemental fluctuation and oxygen octahedral distortion-dependent charge distribution in high entropy oxides. *Nat. Commun.* 13, 2358 (2022).
- 168. Gadre, C. A. et al. Nanoscale imaging of phonon dynamics by electron microscopy. Nature 606, 292–297 (2022).
- Li, L. et al. Observation of strong polarization enhancement in ferroelectric tunnel junctions. Nano Lett. 19, 6812–6818 (2019).
- Repp, J., Meyer, G., Stojković, S. M., Gourdon, A. & Joachim, C. Molecules on insulating films: scanning-tunneling microscopy imaging of individual molecular orbitals. *Phys. Rev. Lett.* 94, 026803 (2005).
- Gross, L. et al. High-resolution molecular orbital imaging using a p-wave STM tip. Phys. Rev. Lett. 107, 086101 (2011).
- Han, Z. et al. Imaging the halogen bond in self-assembled halogenbenzenes on silver. Science 358, 206–210 (2017).

Acknowledgements

This work was supported primarily by the Department of Energy, Office of Basic Energy Sciences, Division of Materials Sciences and Engineering under grant number DE-SC0014430, and partially by the National Science Foundation under grant number DMR-2034738.

Author contributions

The authors contributed equally to all aspects of the article.

Competing interests

The authors declare no competing interests.

Additional information

Correspondence should be addressed to Wenpei Gao or Xiaoqing Pan.

Peer review information Nature Reviews Physics thanks the anonymous reviewers for their contribution to the peer review of this work.

Reprints and permissions information is available at www.nature.com/reprints.

Publisher's note Springer Nature remains neutral with regard to jurisdictional claims in published maps and institutional affiliations.

Springer Nature or its licensor (e.g. a society or other partner) holds exclusive rights to this article under a publishing agreement with the author(s) or other rightsholder(s); author self-archiving of the accepted manuscript version of this article is solely governed by the terms of such publishing agreement and applicable law.

© Springer Nature Limited 2022